THESIS FOR THE DEGREE OF LICENTIATE OF
ENGINEERING
IN
THERMO AND FLUID DYNAMICS

Computational study of rivulets using Volume of Fluid

TOBIAS TIVERT

Division of Fluid Dynamics

Department of Applied Mechanics

CHALMERS UNIVERSITY OF TECHNOLOGY

Göteborg, Sweden, 2009

Computational study of rivulets using Volume of Fluid
TOBIAS TIVERT

Division of Fluid Dynamics
Department of Applied Mechanics
Chalmers University of Technology
SE-412 96 Göteborg, Sweden

Phone: +46-(0)31-7721400
Fax: +46-(0)31-180976

Computational study of rivulets using Volume of Fluid

TOBIAS TIVERT

Division of Fluid Dynamics
Department of Applied Mechanics
Chalmers University of Technology

Abstract

This thesis focuses on numerical methods of soiling and some multi-phase concepts related to it. The Volume of Fluid method was tested in two different test cases and showed fairly good results.

The first test case was a gravity driven rivulet on an inclined plate, where it was an inlet with a constant water velocity at the beginning of the plate. We tested three different grids and five different discretization schemes for the interface equation, and it was found that the sharpest and most accurate one was the Young scheme.

The second was a wind driven rivulet on a flat plate. The experiment setup is a $20mm$ thick, $260x300mm^2$ plate with a 1mm circular water inlet centered on top of the plate. Ambient air flows on both sides of the plate. As the water is introduced, the ambient air will form a rivulet that travels towards the trailing edge of the plate. The rivulet breaks up at the trailing edge, forming droplets of sizes that depend on the flow rate and velocity of the ambient flow. The hole was moved 1 cm upstream of the edge to avoid the rivulet from breaking up on the plate. The results were good for the droplet size and velocity. The sharpest scheme did not converge at all, and thus the HRIC scheme was used instead of the Young scheme.

Keywords : Rivulet, Break-up, VOF, multiphase

Nomenclature

Latin symbols

$\vec{u}$	velocity vector
C	Mass concentration
C_D	Drag coefficient
D	Diameter
f	Drag factor
$\vec{F}$	Momentum Force vector
F_i	Body force
g	Gravity
M	Mass
r	radius
Re_r	Local Reynolds number for the particle
St_v	Stokes number
T	Torque
u_c	Velocity for the carrier phase
u_d	Velocity for the discrete phase
V	Volume
V_d	Volume contains by the discrete phase (particle/droplet)

Greek symbols

α	Volume fraction
μ_c	Viscosity for the carrier phase (fluid)
ρ_c	Density for the carrier phase
ρ_d	Density for the discrete phase
σ	Surface tension
τ_f	Characteristic time scale of the flow
τ_v	Particle response time

Abbreviations

CFD	Computational Fluid Dynamics
CFL	Courant-Friedrichs-Lewy
DNS	Direct Numerical Simulation
VOF	Volume Of Fluid
DCA	Dynamic Contact Angle

|	
UD	Upwind Differencing
DD	Downwind Differencing
CSF	Continuum Surface Force
HRIC	High Resolution Interface Capturing

Contents

Chapter 1

Introduction

1.1 Motivation

THE goal of the project is to numerically simulate soiling on the side view mirror glass and the side window of a car. Modeling the soiling of side windows caused by the side rear view mirrors is of great importance in the car industry. As that the soiling of the side windows diminishes drivers visibility of the mirror.
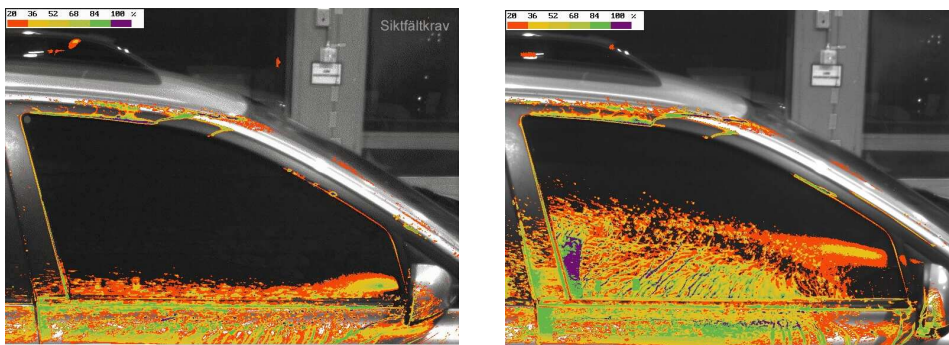
Figure 1.1: The goal is to predict the same results as in the experiment

Simulating the water behavior on a side rear view mirror and on the glass requires a method that is able to track a surface between water and air. However, upstream and downstream of the mirror, we are only interested in the transport of the particle.

1

1.2 Approach

Our approach is to use Lagrange particle tracking, where the shape of the droplets is unimportant before the water hits the mirror and after the droplets have release from the mirror. Volume of fluid is used at the mirror, where we need to know the shape of the droplet/rivulet.

Volume of fluid has many advantages. It can handle the shape of the droplet/rivulet, the surface tension is present, and break-up and coalescence work by definition. It has however some major disadvantages as well; the simulation takes a very long time and is unstable if the surface tension is high.

Chapter 2

Interface tracking methods

Interface tracking methods are used in the case of two or more fluids that are well separated by an interface, such water and air. There are mainly two different kinds of methods, front tracking and volume methods. The volume method is in this case volume of fluid (VOF).
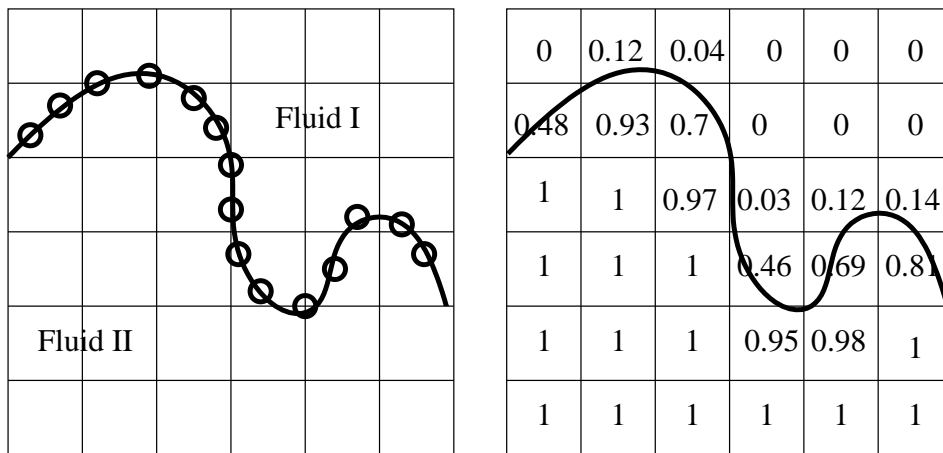
0	0.12	0.04	0	0	0
0.48	0.93	0.7	0	0	0
1	1	0.97	0.03	0.12	0.14
1	1	1	0.46	0.69	0.8
1	1	1	0.95	0.98	1
1	1	1	1	1	1

Figure 2.1: front tracking and VOF method

2.1 Front tracking

In front tracking, mass less particles can be used to separate the different fluids. To track the interface, an evolution equation is solved to reconstruct the front at the new location; see Fig 2.1. The advantage is that the interface remains sharp during the iterations and the methods are also very accurate. The main drawback is that constraints

3

must be specified for break-up and coalescence, and there must be very many particles, which can slow down the computation; see Univerdi & Tryggveson (2001).

2.2 VOF

In VOF, a color function , α, is used instead of particles to separate the different fluids, where α is between 0 and 1; see Fig 2.1. VOF can handle different droplet shapes, break-up and coalescence, and surface tension is also included. The equations are fairly simple. One set of momentum and continuity equations and an interface tracking equation, which is simply a convection equation are, solved. The equations are given as

$$\frac{\partial}{\partial t}\rho u_i + \frac{\partial}{\partial x_j}(\rho u_i u_j) = -\frac{\partial p}{\partial x_i}$$
$$+\frac{\partial}{\partial x_j}\left[\mu\left(\frac{\partial u_i}{\partial x_j} + \frac{\partial u_j}{\partial x_i}\right)\right] + \rho g_i + F_{\overline{\sigma}} \tag{2.1}$$
$$\frac{\partial u_j}{\partial x_j} = 0$$

The fluid properties are calculated as

$$\rho = \alpha_2 \rho_2 + \alpha_1 \rho_1$$
$$\mu = \alpha_2 \mu_2 + \alpha_1 \mu_1 \tag{2.2}$$

where α is an indicator function that identifies which of the fluids is in the cell.

$\alpha_i = 0$ if the cell is empty of fluid i

$\alpha_i = 1$ if the cell is full of fluid i

$0 < \alpha_i < 1$ if the cell contains both fluids

The relation for the indicator functions must fulfill

$$\sum_{i=1}^{2} \alpha_i = 1 \tag{2.3}$$

Since there are only two phases in the present application (water and air), we need only solve for one indicator, α. The indicator function equation is simply a scalar transport equation for the interface.

$$\frac{\partial \alpha}{\partial t} + \frac{\partial \alpha u_i}{\partial x_i} = 0 \tag{2.4}$$

Term $F_{\vec{\sigma}}$ in the momentum equation denotes surface tension. FLUENT uses the CFS of Brackbill *et al.* (1992) for the calculation of surface tension, and the term has the form

$$\vec{F_{\sigma}} = -(\sigma \bigtriangledown \alpha) \bigtriangledown \cdot \left(\frac{\bigtriangledown \alpha}{|\bigtriangledown \alpha|} \right) \tag{2.5}$$

This term is very large at the interfaces, which is the main reason why VOF simulations are numerically very unstable. An accurate solution requires sharp interfaces, but unfortunately the sharp interfaces make the equations numerically unstable. Hence we cannot afford interfaces that are too sharp.

The equations stay reasonably stable for droplet sizes down to a couple of centimeters but become very unstable for droplet sizes of a couple of millimeters. In this work, we tried to reach a compromise: we use a discretization scheme for the α equation that is fairly stable.

2.3 HRIC

There are many different VOF schemes, such as the old doner-acceptor scheme (see Hirt & Nichols (1981)), the more accurate geometric Reconstruction scheme (see Youngs (1982)) and the more popular compressive schemes CICSAM (see Ubbink (1997)).

The modified HRIC scheme consists of a non-linear blending of upwind and downwind differencing. It was developed by Muzaferiju & Peric (2000) and is a compressive scheme like CICSAM.

Pure upwind will be bounded but is too diffusive. Downwind is unstable but not diffusive so the combination is suitable for VOF calculations. The normalized volume fraction $\overline{\alpha_c}$ in the cell center is computed as

$$\overline{\alpha_c} = \frac{\alpha_c - \alpha_u}{\alpha_d - \alpha_u} \tag{2.6}$$

Subscripts u, d and c in Fig. 2.2 denote upstream, downstream and the actual cell, respectively. With $0 < \overline{\alpha} < 1$, the face value of α is computed as

$$\overline{\alpha_f} = \begin{cases} \overline{\alpha_c} & \text{if } \overline{\alpha_c} < 0 \\ 2\overline{\alpha_c} & \text{if } 0 < \overline{\alpha_c} < 0.5 \\ 1 & \text{if } 0.5 < \overline{\alpha_c} < 1 \\ \overline{\alpha_c} & \text{if } 1 > \overline{\alpha_c} \end{cases}$$

Direct use of $\overline{\alpha_f}$ can cause wiggles at the interface if the flow is parallel to the interface. To prevent this the HRIC scheme uses the
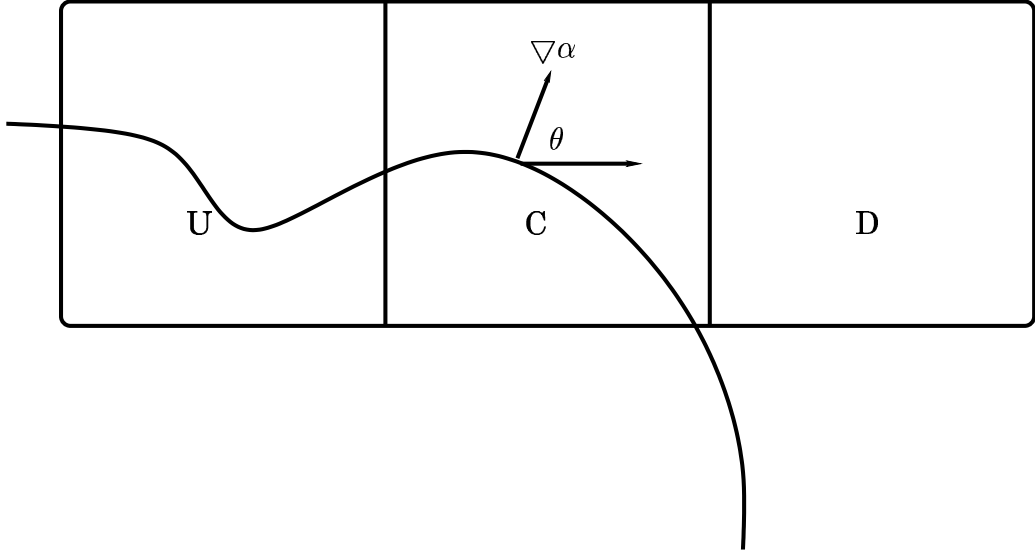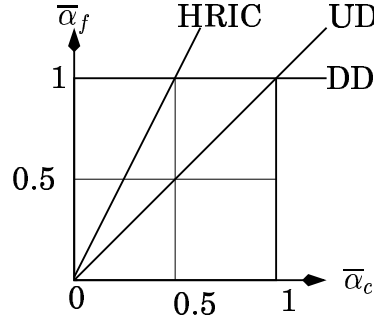
Figure 2.2: The HRIC discretiztion scheme

Figure 2.3: cell

angle between the interface and the normal vector to the grid face. $\overline{\alpha}_f$ is corrected as

$$\overline{\alpha}_f^* = \overline{\alpha}_f \sqrt{cos\theta} + \overline{\alpha}_c(1 - cos\theta)$$

If the local Courant number, Co, is too large, convergence problems may be encountered. HRIC also takes into account high local Co, and thus the face value of α_f is corrected as

$$\overline{\alpha}_f^{**} = \begin{cases} \overline{\alpha}_f^* & \text{if } Co < 0.3 \\ \overline{\alpha}_c & \text{if } 0.7 < C_o \\ \overline{\alpha}_c + (\overline{\alpha}_f^* - \overline{\alpha}_c)\frac{0.7 - Co}{0.4} & \text{otherwise} \end{cases}$$

Here, Co is defined as

$$Co = \frac{\vec{v} \cdot \vec{n} S_f \Delta t}{V_f}$$

Finally we obtain the HRIC scheme

$$\alpha_f = \gamma \alpha_c + (1 - \gamma)\alpha_D$$

where γ is defined as

$$\gamma = \frac{(1 - \overline{\alpha}_f^* *)(\alpha_D - \alpha_U)}{\alpha_D - \alpha_c}$$

The HRIC scheme is implemented in Fluent (2006).

Chapter 3

Drag of a sphere

As mentioned in Chapter 1 we want to change from VOF to Lagrange after the droplet has left the mirror. But when should we make the change? One criterion must be when the resolution of the droplet is too poor in terms of drag prediction. Furthermore, it is good if the droplets do not break-up any more so that we do not need any break-up model during the tracking. We know the break-up stops at a Weber number, approximately 12. From the experiment of Lafuente (2007) that the droplet stops to breaking up just a couple of centimeters from the mirror. In the present study we cover the Reynolds number range relevant to flow around a mirror. We test all Reynolds numbers that are interesting, and we know the droplet size, and the droplet and wind speed. The interesting area is Reynolds numbers from 10 - 1000.

3.1   Domain, boundary condition and grid

The domain size will influence the drag if it is too small. From an earlier study we know that the domain should not be less than $6 \times 12 \times 6 mm^3$. Symmetric boundary conditions are used at the low and high z and y boundaries. We use constant velocity the inlet (low x), and a Neumann condition is used at the outlet (high x). The different resolutions of the sphere were 2, 4, 8 and 16 cells covering the sphere.

3.2   Results

The simulations do not use any kind of turbulence models because no turbulence model will be used in the VOF simulations. All the simulations were made with a second-order upwind scheme and the SIMPLE algorithm. As can be seen in Fig. 3.1, the results are fairly good even
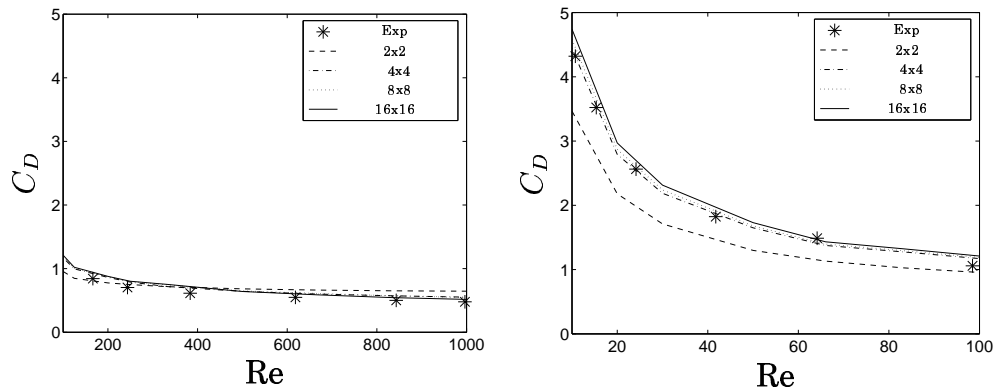
Figure 3.1: Experiment and CFD calculation of drag on a sphere

for the low resolutions. For the higher Reynolds numbers this can be explained by the pressure drag and that the shape is not very important.

However, for lower Reynolds numbers, the viscous drag is high and we do not have any explanation for why it is so good. This means that in practical cases we do not need to give very much attention to the resolution of the droplets. It seems that it is sufficient to resolve a sphere by 4 cells in each direction.

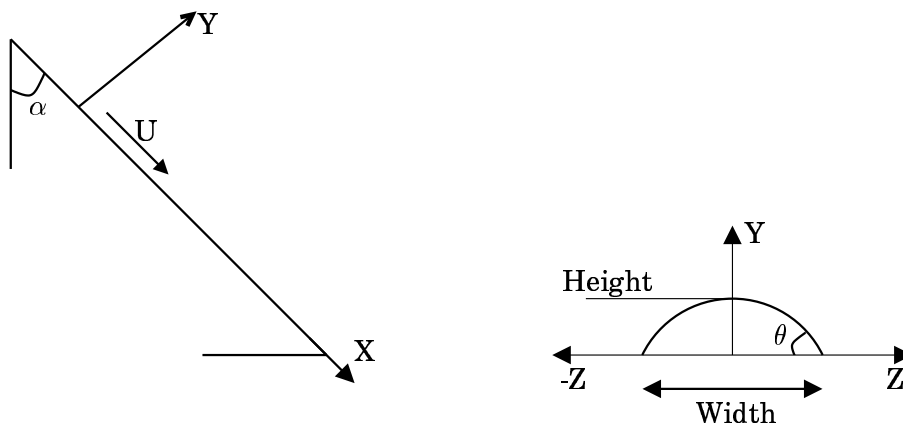# Chapter 4

Gravity driven rivulet

4.1 Introduction

Figure 4.1: schematic picture of the plate and the rivulet

4.2 Domain and Grid

The computational domain has the dimensions $85 \times 15 \times 10mm^3$. The width of the plate has have been reduced so that it is only ten times the diameter of the rivulet in the spanwise direction. It was found that the outlet boundary condition influenced the rivulet upstream independently of which boundary condition we choose. This led us to introduce a step $50mm$ downstream of the inlet in order to reduce any influence of the outlet boundary condition; see Fig. 4.2.

In this way there will be a small bump at the step and a small pressure disturbance caused by the curvature. However, this dies out more quickly than the disturbance caused by the outlet boundary condition.

11

An isotropic hexahedrial mesh is chosen at the location of the rivulet; the area is 3.4 mm wide and 1mm high, and it is stretched by 5% outside this area. The baseline mesh is a 4×4 mesh that covers the cross section of the rivulet; for the 8×8 mesh an adaption is made in a region two times the rivulet width and height and this procedure is repeated for the 16×16 case.
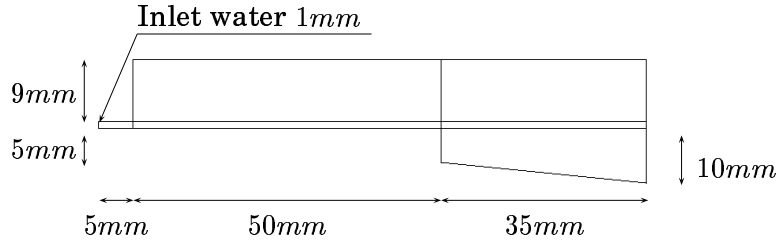
Figure 4.2: Configuration 1
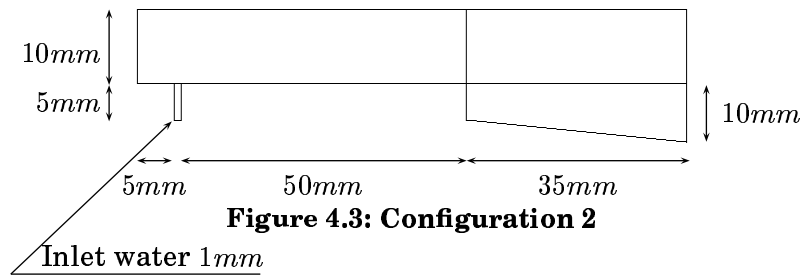
Figure 4.3: Configuration 2

4.3 Boundary conditions

Symmetry boundary conditions were applied at the spanwise boundaries (low and high z). The flow rate is taken from an experiment (Ataki & Bart (2004)). Neumann boundary conditions are prescribed at the outlet and at the top (high y). The static contact angle in the VOF model was also taken from the experiment and was set to 66.5^o

The baseline case is set up as:

Grid resolution:	4 cells over the inlet
VOF scheme:	Geometric Reconstruction (Young)
Velocity discretization:	Second-order upwind
Pressure discretization:	PRESTO
Pressure-velocity coupling:	PISO
Static contact angle:	66.5^o
Slope of the plate:	$\alpha = 24.5^o$

4.4   Results and Discussion

The baseline case was used for the different mass flow rates. The predicted rivulet broke up for mass-flow below $28ml/min$, while it did not in the experiment . However if we locate the hole so that water enters from the bottom, see Fig. 4.3, we also obtain a stable rivulet for the lower mass flow rates. However, it still begins to breaks up too early compared with experimental data. In the experiment it begins to break-up at $8ml/min$ whereas in the simulations it breaks up at already $19ml/min$. The explanation for the early break-up is probably numerical disturbances. The reason for the early breakup may also be that the VOF method does not include all physics, such as dynamic contact angle, wet/dry surface etc. A typical snapshot of the rivulet is shown in Fig. 4.4.
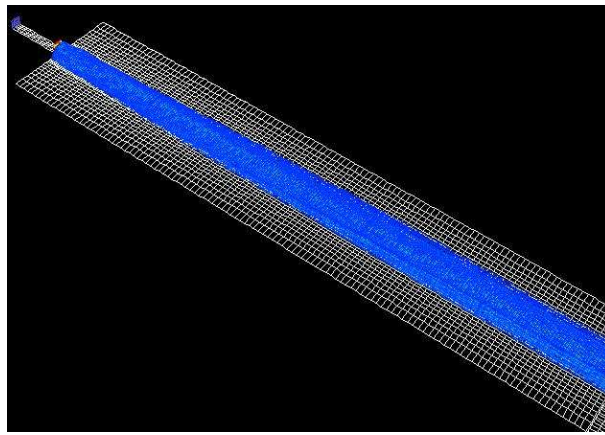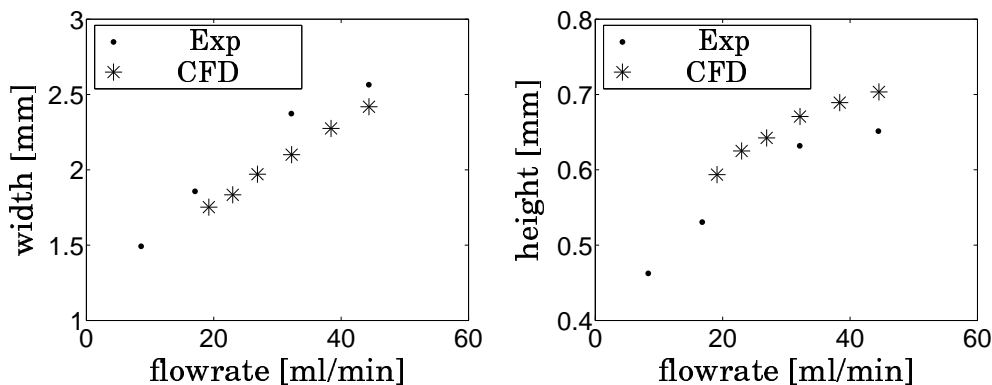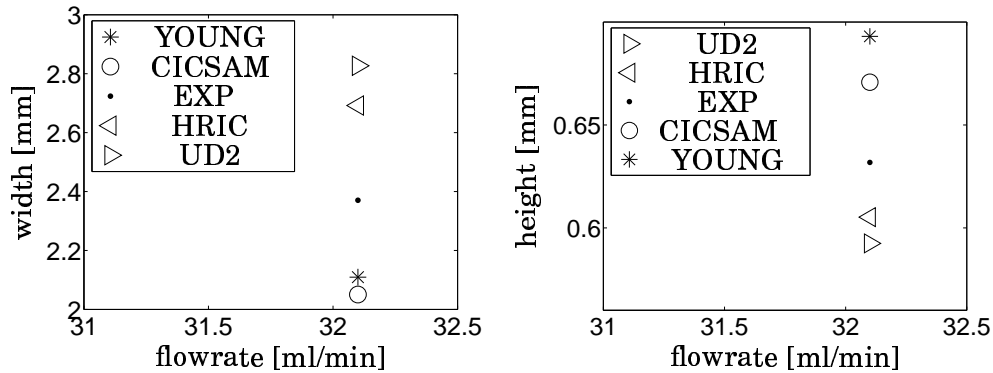

Figure 4.4: Snapshot of the rivulet

Figure 4.5: Baseline grid. Predictions and measurements(Ataki & Bart (2004)) of the width and height of the rivulet for different mass flow rates.

Figure 4.5 compares the predicted and measured width and height

of the rivulet for different mass flow rates. As can be seen, the agreement is fairly good, but both the width and height of the rivulet are slightly under-predicted. One reason for this discrepancy can be that the contact angle used in the simulations was that measured on a droplet at rest, and this angle changes slightly when the rivulet is moving. The maximum discrepancy between the predictions and measurements in Fig. 4.5 is approximately 15%.
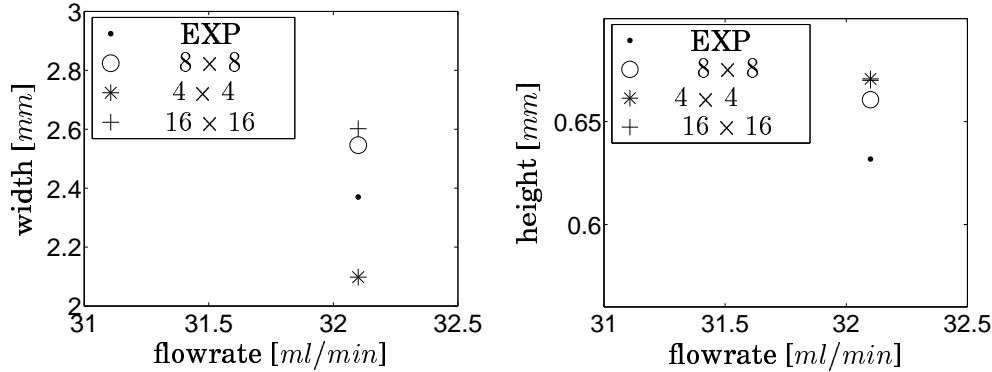

Figure 4.6: Predictions and measurements (Ataki & Bart (2004)) of the width and height of the rivulet for different discretization schemes. The baseline case is used for the simulations except that a different scheme is used.

The influence of different discretization schemes in the α equation is presented in Fig. 4.6. As can be seen, the influence in this simple test case is rather small. The largest difference between the schemes is that the interface is thinner in Young's scheme compared with the others. However, all schemes predict the center of the interface in fairly close agreement with experiments.
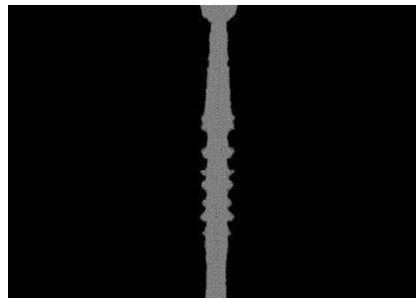

Figure 4.7: Young's scheme with the finest mesh of $16x16$ cells. View from above the plate.

For the case in which $16x16$ cells cover the cross section of the rivulet, the simulation become very unstable almost directly, and this effect can be seen in Fig. 4.7. The two other grids, 4×4 and 8×8, did not show

Figure 4.8: Predictions and measurements (Ataki & Bart (2004)) of the width and height of the rivulet using different grids. Note that the HRIC scheme was used for the finest grid, 16×16.

any great difference; see Fig. 4.8. The results obtained with the 16×16 grid were in this case computed with the more diffusive (and stable) HRIC scheme.
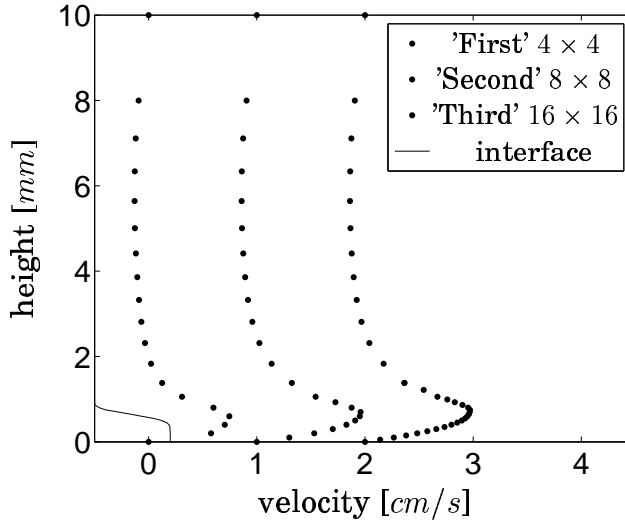
Figure 4.9: Velocity profile. The grid distribution is illustrated by the markers

Figure 4.9 presents the velocity profiles. To enhance visibility, the different profiles are translated in the horizontal direction; the 4×4, the 8×8 and the 16×16 profile start at zero, $1m/s$ and $2m/s$, respectively. We gain of course the best resolution of the boundary layer with the 16×16 grid; see Fig. 4.9. It should be noted that the max velocity increases when we refine the grid but that the mass flow stays constant; see Fig 4.8. However, the shape of the rivulet differs a great deal. It can also be seen that we have refined the grid only in the most important area, but both the water and air boundary layers are located within the refined

15

area.
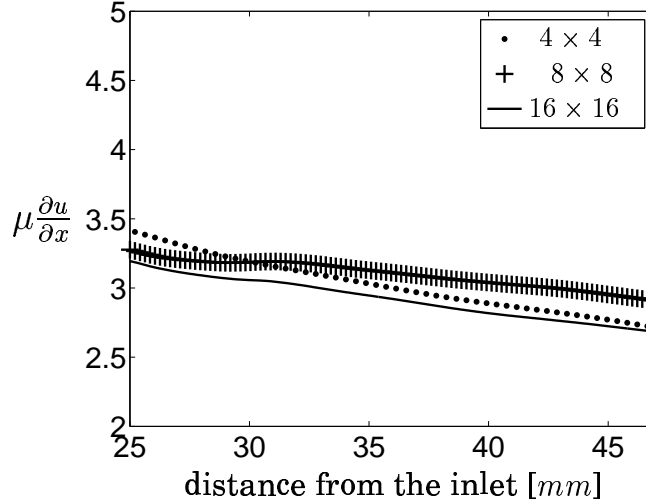
Figure 4.10: Wall shear stress

The wall shear stress is almost the same for the three grids, see Fig. 4.10. However, as can be see in Fig. 4.10, the shear stresses are not constant in the streamwise direction, which we should perhaps have expected. This explains why we get different solutions for the cases with the inlet from below and the ordinary one, see Figs. 4.2 and 4.3. When we used the original inlet (see 4.2) break-up occurred much earlier compared with the case of the inlet from below. If the flow were fully developed (defined as $\partial u/\partial x = 0$) there it should be no difference using the two different inlet boundary conditions. However, since the wall shear stress varies in the streamwise direction, the flow will be affected by the inlet condition.

4.5   Instabilities

Numerical instabilities were encountered with the use of the VOF algorithm. There are several reasons that explain why the VOF algorithm is unstable.

- We take derivatives of dependent variables that are discontinuous at the interface.

- The surface tension term is highly non-linear.

- The pressure difference at the interface can be estimated as

$$p_{in} - p_{out} = \frac{\tau}{R}$$

where τ denotes the surface tension.Hence can the pressure difference of the interface, $p_{in} - p_{out}$, becomes very high when the dimension, R, of the rivulet is small.

- The Rhie & Chow interpolation may cause numerical problems at the interface when large body forces are present in the momentum equations.

- If the terms for pressure difference and the surface tension are much larger than the other terms in the momentum equation (as is indeed the case, see below), spurious velocities near the interface may appear if the iterative the solution is not extremely well converged at each time step.
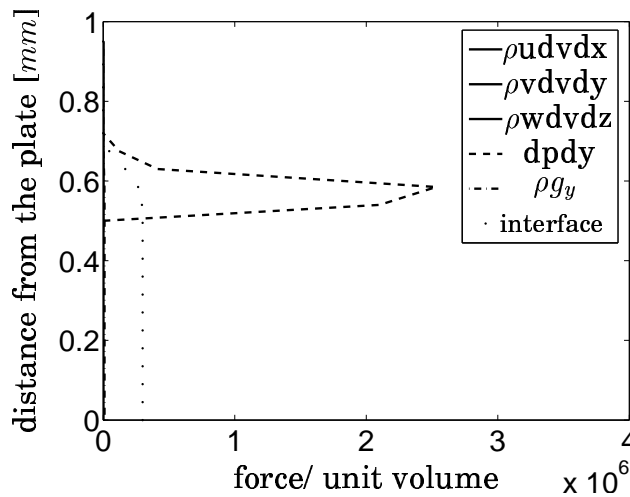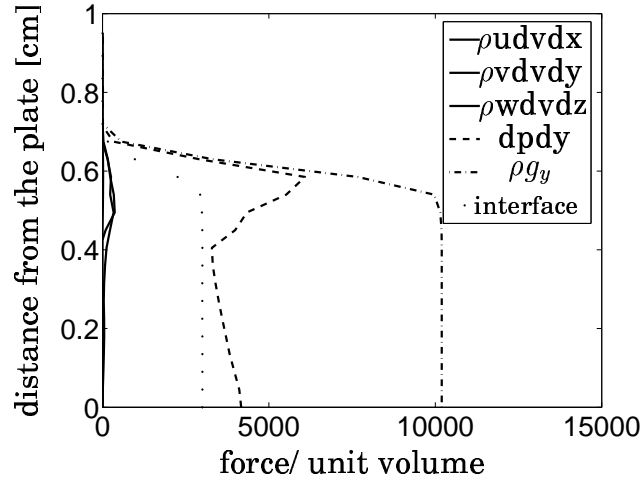

Figure 4.11: Different terms in the wall-normal momentum equation

Different terms in the momentum equation are compared in Fig. 4.11. The maximums of the different terms are:

max(ρudvdx):   41
max(ρvdvdy):   954
max(ρwdvdz):   210
max(dpdz):   2 530 000
max(ρg):   10 200

The pressure term is approximately 250 times larger than the second largest term, and it must be balanced by the surface tension term (the diffusion terms are very small). If the iterative solution at one time step is not well converged, it will result in spurious velocities. In the present study, the height of the rivulet is approximately $0.5mm$; see Fig. 4.5.

If the rivulet is ten times larger ($0.5cm$ instead of $0.5mm$) the numerical problems disappears; the pressure difference is much smaller, the velocities are higher, and hence the difference between the terms is much smaller, see Fig. 4.12. The simulation converges faster and all numerical problems are almost gone.

Figure 4.12: Different terms in the wall-normal momentum equation for rivulet 10 times larger

The maximums of the different terms in Fig. 4.12 are:

max(ρudwdx):	19
max(ρvdwdy):	369
max(ρwdwdz):	335
max(dpdz):	6 090
max(ρg):	10 200

Now we see that the differences between the terms are much smaller, which gives much better numerical stability.

As we have seen, the stability is a great problem in VOF when the dimension of the rivulet is small. The general aim is to use a discretization that is as good as possible in order to achieve a sharp interface but, when the dimension of the rivulet is of the order of one millimeter, it can not be too sharp because we will then encounter numerical problems. The best choice in this case seems to be the more diffusive HRIC scheme.

For industrial flow cases we are usually forced to use unstructured meshes because of the high geometrical complexity. Preliminary tests have been made with Young's scheme on an unstructured mesh and it was found that it diverges directly. The HRIC scheme, however, works well, see Fig. 4.13. This scheme seems to be a good compromise between accuracy and stability.
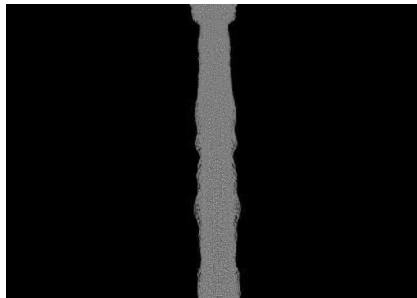
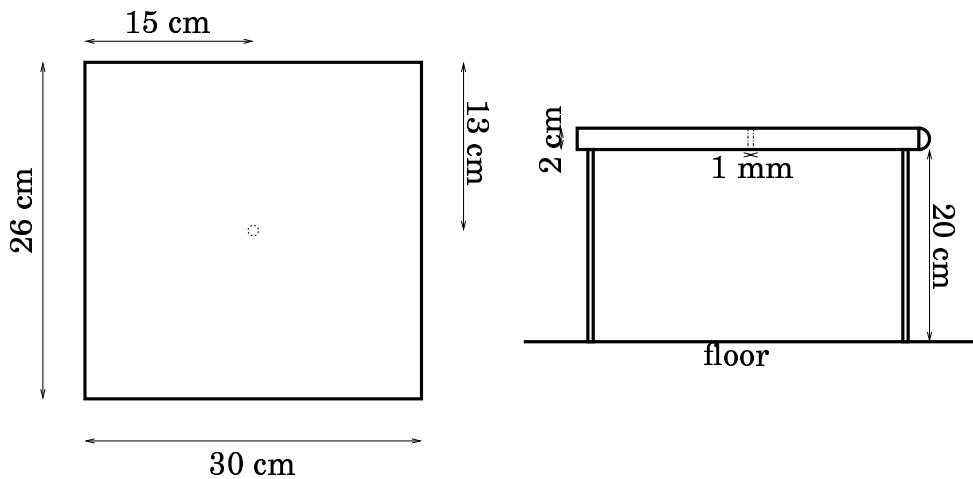**Figure 4.13: HRIC at unstructured mesh (tetrahedral)**
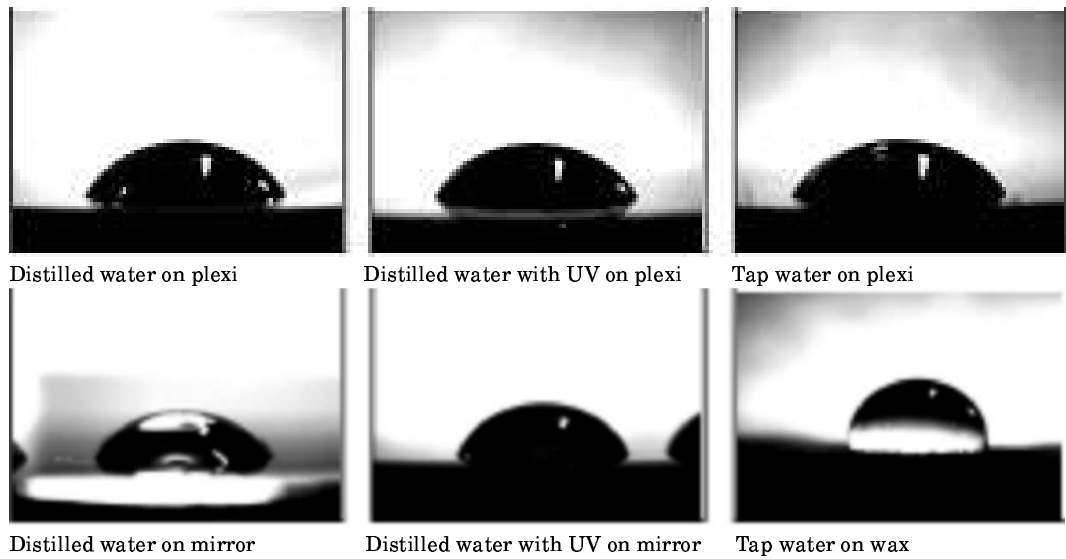
Chapter 5

Shear driven rivulet

5.1 Experimental Study

The main interest in the experiment was to register the radius and velocity of the released droplets at different distances from the trailing edge. Schematic pictures of the experiment dimensions are shown in Fig. 5.1.

Figure 5.1: Plate used in the experiment from above and from the side

The static contact angle was also measured. The experimental equipment was a high-speed camera with a resolution of 256×256. A still picture camera was also used, with a resolution of 9M pixels. This was mainly used when the rivulet (droplet) was stationary. The first measurement made was of the static contact angle. Figures 5.2 and 5.3

| Distilled water on plexi | Distilled water with UV on plexi | Tap water on plexi |
| Distilled water on mirror | Distilled water with UV on mirror | Tap water on wax |

Figure 5.2: Static contact angle of different liquids and solids

Figure 5.3: Measurement of the static contact angle

are photos taken at two different locations on the plate for different liquids.

The analysis of the contact angles was carried out in photoshop and the values are given in Table 5.1.

The velocity and size of the released droplets were obtained by high-speed filming UV liquid in order to obtain sharper pictures. The pictures were analyzed in Matlab with a, image toolbox where the movement of each centroid was detected. The velocities of the droplets were obtained by multiplying with the camera frequency. The measurements were repeated ten times for each water flow rate and ambient air flow to obtain good statistics. The duration of each film was two seconds with a frequency of 1000 Hz.

	Specimen left (degrees	Contact angle right (degrees)	Mean (degrees)	Estimated error	Relative error
Distilled water on mirror	57.6	62			
Distilled water on mirror2	59	64.8	61	8	0.13
Distilled water and UV on mirror	57.6	62			
Distilled water on mirror2	59	64.8	61	8	0.13
Distilled water on plexi	60.4	61.4			
Distilled water on plexi2	58	59.7	60	8	0.13
Distilled water on and UV plexi	59.8	56.7			
Distilled water on and UV plexi2	61.5	62.7	57	8	0.13
tap water plexi	58.3	60.1			
tap water plexi2	55.3	54.8	60	8	0.13

Table 5.1: Contact angles for some combination of liquids and solids

Corrections have been made for measurements errors, such blurriness and converting between different formats. Greater detail on the experimental work is given in Lafuente (2007).
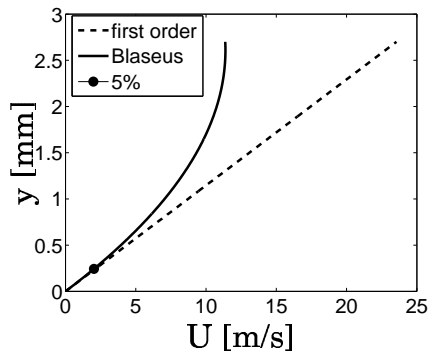
5.2 Domain

The computational domain has the dimensions $400 \times 80 \times 21 mm^3$. It was necessary to include the entire plate in the computational domain in order to correctly predict the boundary layer growth. The width of the plate has been reduced, and thus the computational domain extends one centimeter at each side of the hole (the diameter of the hole is one millimeter). The reduction of the computational domain is not expected to have any effect on the predicted results.

5.3 Boundary conditions

Symmetry boundary conditions are applied in the spanwise boundaries (low and high z) and at the bottom and top (low and high y). The air speed is set to $11.1 m/s$ at the inlet (low x). The speed of the water through the hole in the middle of the plate is set to $0.23 m/s$. Neumann boundary conditions are prescribed at the outlet.In the VOF model, the static contact angle that defines the angle between the wall and the surface of the rivulet needs to be presented. The static contact angle is set to 60°.

5.4 Grid

The grid that was used consists of 4.4 million cells. The quality of the mesh was perfect when a pure hexahedral mesh was used. A finer mesh was used at the expected location of the rivulet. The first node is set in the "linear layer" of the Blasius profile and this node is consequently located approximately $0.3mm$ from the wall; see Fig. 5.4. However, since our earlier work indicated that a rivulet must be resolved by at least four cells, the first cell is located $0.2mm$ from the wall.

Figure 5.4: First node in the "linear layer"

The cells are $0.2 \times 0.2mm^2$ in the $y - z$ plane in a box that extends the entire domain in the x direction, and the size of the box is $8 \times 8mm^2$. Outside the box, the grid is stretched by 3% in the spanwise (z) direction. The grid in the streamwise direction (x) is stretched from the hole to the inlet by 4%.The grid spacing is constant from the hole to the edge, and 1% streching is used downstream of the edge.
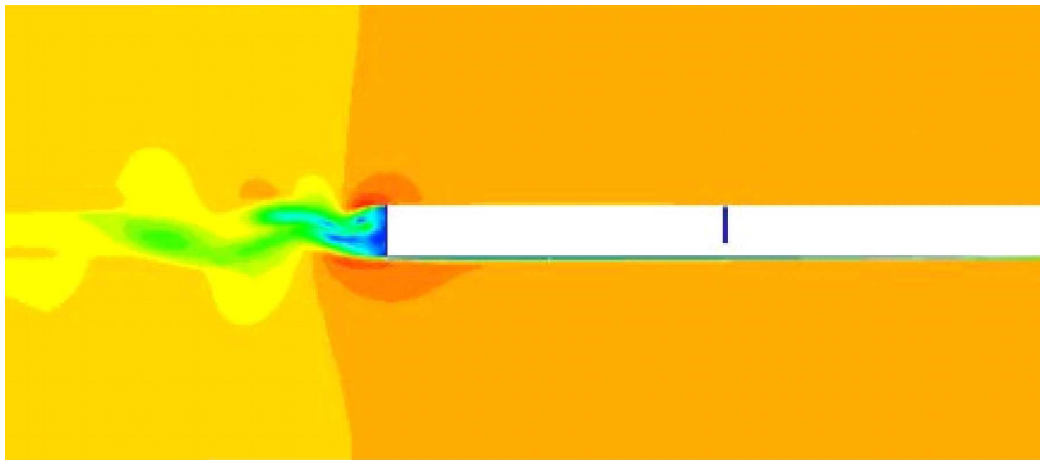
Figure 5.5: Snapshot of the velocity field. Flow from right to left.

The U velocities along the upper of the plate are shown in Fig. 5.6 and, as can be seen, they agree well with the Blasius profiles.
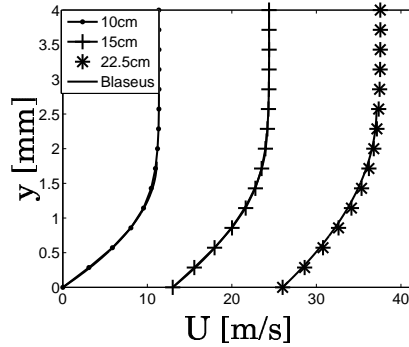

Figure 5.6: Computed and analytic laminar boundary layer at different distances from the inlet

5.5 Results and Discussion

In our previous investigation of the gravity driven rivulet simulations we found that the predicted break-up of the the rivulet took place too early as compared to experiments. We thus decided in the present work to simulate the highest water flow rate and the lowest air velocity. It turns out that the rivulet breaks up in this case as well. This may be a resolution problem. The fine grid (cells of $0.1mm$; the baseline grid has cells of $0.2mm$) shows better tendencies, but it was impossible to obtain a converged solution even when 40 iterations per time step and a Co number of 0.2 were used. One reason is that the rivulet moves too fast. The only force that acts to reduce the speed of the rivulet in the simulation is the shear stress between the water and the solid wall. In reality, many more physical processes come into play, such as the difference in contact angle, wetting properties, roughness etc. In the case of a droplet, the dynamic contact angle (DCA) has great importance for the velocity, but it will not have that great an impact on the speed in the case of a rivulet. The pressure difference over a droplet is caused by the difference in surface curvature at the back and front sides. A rivulet has only a front side, and no back side, and hence the effect of increasing the dynamic contact angle is similar to that of increasing the static contact angle.

Several modifications were tested to prevent break-up of the rivulet.

1. First, the initial boundary conditions were modified so that the rivulet was defined at the plate at time zero. This did not help,

and the rivulet broke up anyway; it simply took place somewhat later.

2. Second, we increased the wall shear stress of the rivulet to decrease its speed. The physical argument was that we introduced surface roughness of the wall by increasing the viscosity. The lowest viscosity at which the rivulet did not break-up was six times the physical viscosity. One advantage in modifying the viscosity is that the Weber number, which governs the break-up, does not change. We believe that increasing the viscosity does not have any large negative effect since the VOF model , even when using the physical viscosity, over predicts the speed of the rivulet.

3. Third, we moved the hole closer to the edge using the physical viscosity. The hole was placed one centimeter from the edge. In this way, the rivulet does not break-up.

We decided to run the simulations with a hole close to the edge (the third alternative above) because we are primarily interested in the break-up process. A break-up upstream of the edge would most likely affect the frequency of the rip-off at the lower corner of the edge. The rip-off frequency would probably be governed by the frequency of the rivulet break-up on the plate, and that would affect the size of the droplets leaving the lower corner of the edge.

Figure 5.7: A rivulet with physical viscosity, μ

Figure 5.7 illustrates that the rivulet breaks up if no modification is used. When the viscosity is increased by a factor of six (Fig. 5.9), the rivulet does not break-up. Figure 5.8 shows that, when using a finer mesh than the baseline mesh, the rivulet breaks up later but becomes unstable. It is not clear whether this behavior is physically realistic or not.
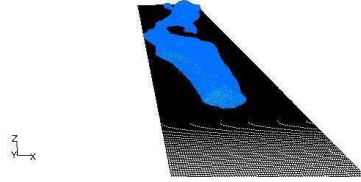
Figure 5.8: Unstable rivulet with fine mesh (cells of $0.1mm$**)**

Figure 5.9: A rivulet with viscosity 6μ
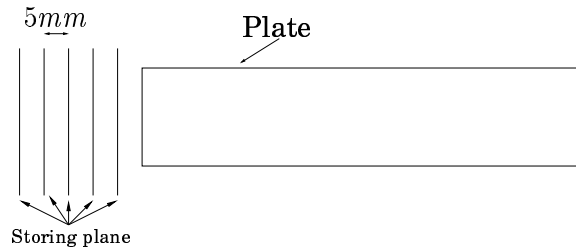
5.6 Data storage

Figure 5.10: Planes with constant x **for storing data**

Instantaneous data must be stored to trace the droplets that are being ripped off at the lower corner of the edge. Due to space limitations, we could not store the complete set of data, and thus a couple of planes were chosen. Five planes with constant x were chosen downstream of the edge separated by $5mm$; see Fig 5.10. The first plane is located $5mm$ downstream of the edge. Another three planes with constant z were selected, see Fig. 5.11, which are separated by $3mm$; the first plane is located at the symmetry plane.

A snapshot series of a droplet moving in the center plane is shown in Figs. 5.13-5.18. Figure 5.13 shows how the ambient flow begins to rip off the droplet from the lower corner of the edge. Nine milli seconds later, the droplet starts to release from the corner, Figure 5.14. Figure 5.15 shows how the droplet at the lower edge is released and how a new
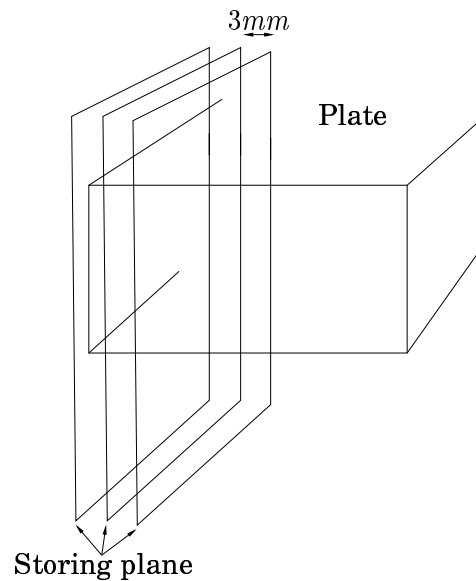
Figure 5.11: Planes with constant y for storing data

droplet begins to form at the upper corner. The shape of the droplet that is released is elongated. In Fig. 5.16 the shape of the droplet has became fairly circular. Figure 5.17 shows how the droplet starts to break-up. Unfortunately, it does not take place in the center plane, and we therefore cannot visualize it to any great degree with our stored instantaneous data. Figure 5.18 shows the droplet when it has reached its final size; it will not break-up any further. It has become two or three small droplets of a similar size as this one.

5.7 Velocity and radius calculation

This sub-section gives an evaluation of the speed and size of the droplets. To locate a droplet in the domain, we need to find a closed area. It is computationally very expensive to do this on an unstructured grid (FLUENT is an unstructured solver). Hence we do it in the following way.

Step 1: Interpolate the data to a Cartesian grid with second-order accuracy.

Step 2: Define a very coarse grid (see Fig. 5.12) where each cell is checked to see whether it contains any volume fraction.

Step3: If there is any volume fraction in the large cell, then an algorithm must find the enclosed area.
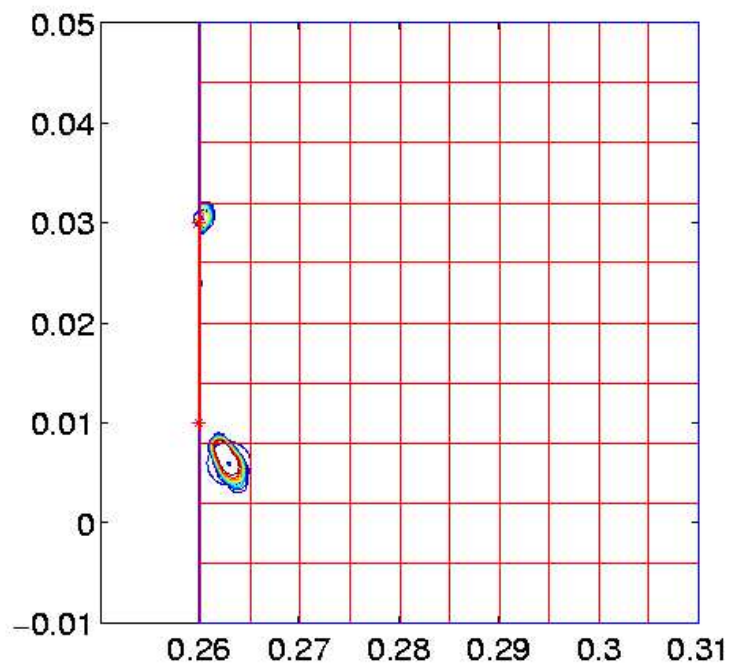
Figure 5.12: The search algorithm, the search mesh and a droplet with its corresponding radius

Figure 5.13: Time $t = t_1$

Figure 5.14: Time $t = t_1 + 9ms$

Step 4: If a droplet covers two or more cells, then a new, large cell is defined. It is not a problem to have more than one droplet in a cell.

Step 5: Compute a corresponding radius of the closed area.

Step 6: Compute the distance between the droplets and divide it by the time step, which gives the speed of the droplet.

The approach described above is carried out in Matlab.

Figure 5.15: Time $t = t_1 + 12m$

Figure 5.16: Time $t = t_1 + 15ms$

5.8 Comparison with experiment

Figures 5.19 and 5.20 present the predicted and the measured radii and velocities of the droplets. The measured data have been averaged over many droplets. We accumulated predicted data that cover the release of three droplets. Hence the predicted results in Figs. 5.19 and 5.20 are presented as scatter plots that cover the three droplets at all time steps.

The predicted radii are somewhat lower than the experimental values. The result is that the velocities of the droplets are over-predicted, since a small droplet accelerates faster than a large one. The discrep-

31

Figure 5.17: Time $t = t_1 + 18ms$

Figure 5.18: Time $t = t_1 + 21ms$

ancy between predictions and experiments is probably due to the too high velocity of the rivulet. This gives too small an accumulation of water before it rips off.

The predicted data at the left hand side of the plots represent droplets that are moving downwards along the vertical edge. It appears as though they are over-represented, but the reason for this is that they are detected at each time step. The releasing frequency in the experiment was $1.619Hz$ and in the simulation $2.04Hz$. This discrepancy illustrates the same problem as before: the predicted velocity of the rivulet is too high. Figures 5.23 and 5.24 illustrate one experiment scatter plot. It covers a two second sequence. The solid lines shows the
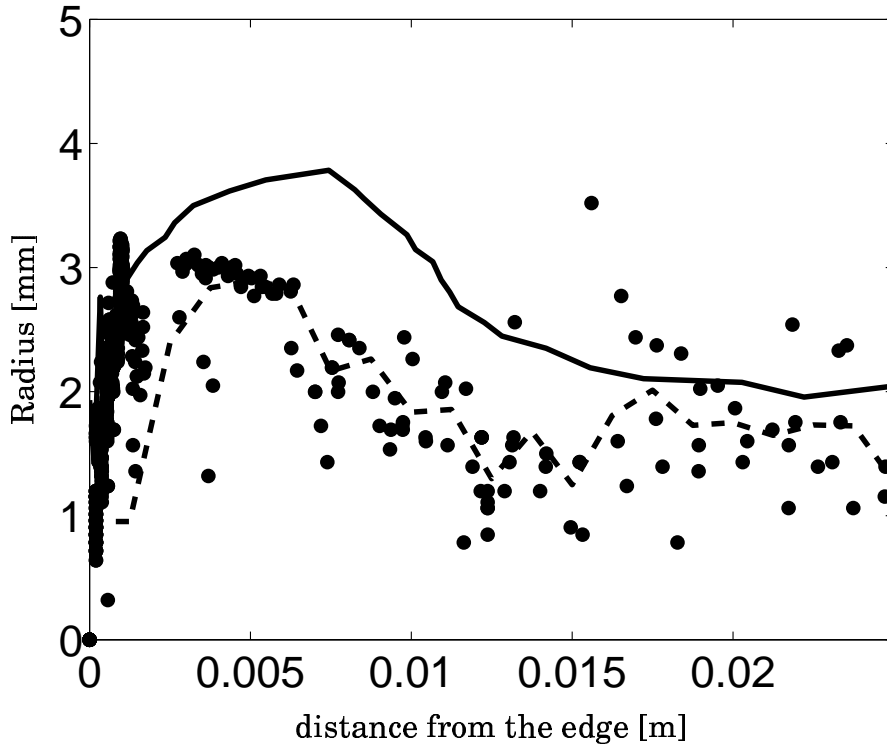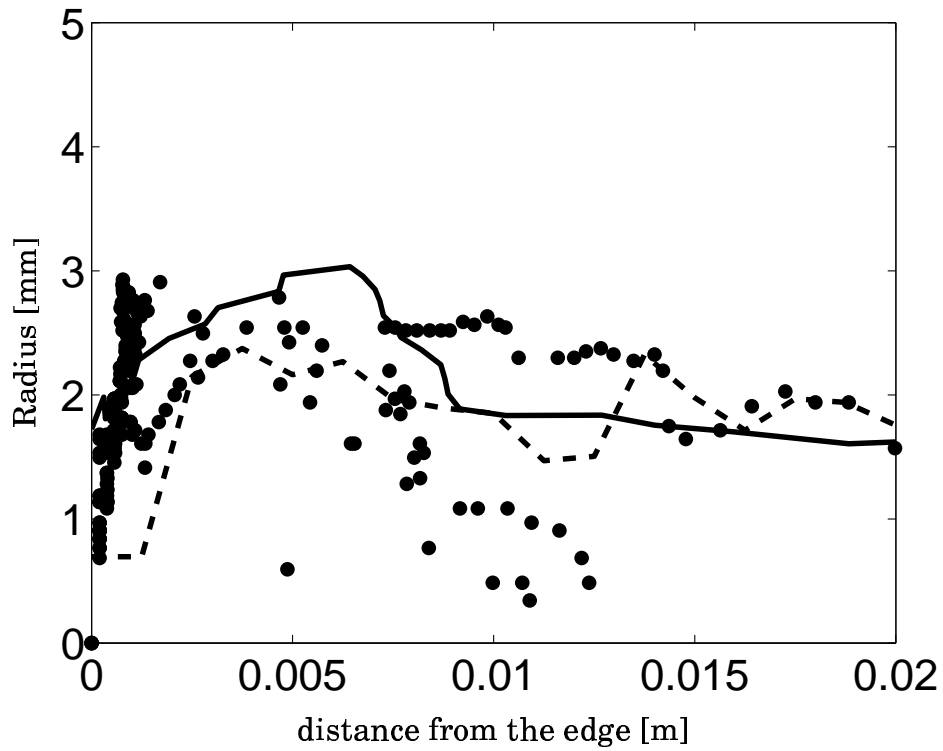
Figure 5.19: Radius of the droplets for 40 km/h. Dots: predictions; dashed line: computed average; solid line: experimental data.

average values with its own average also. It also shows that the average is not the same as for the whole series of experiments. See 5.19 which contains ten experiments of two seconds each.
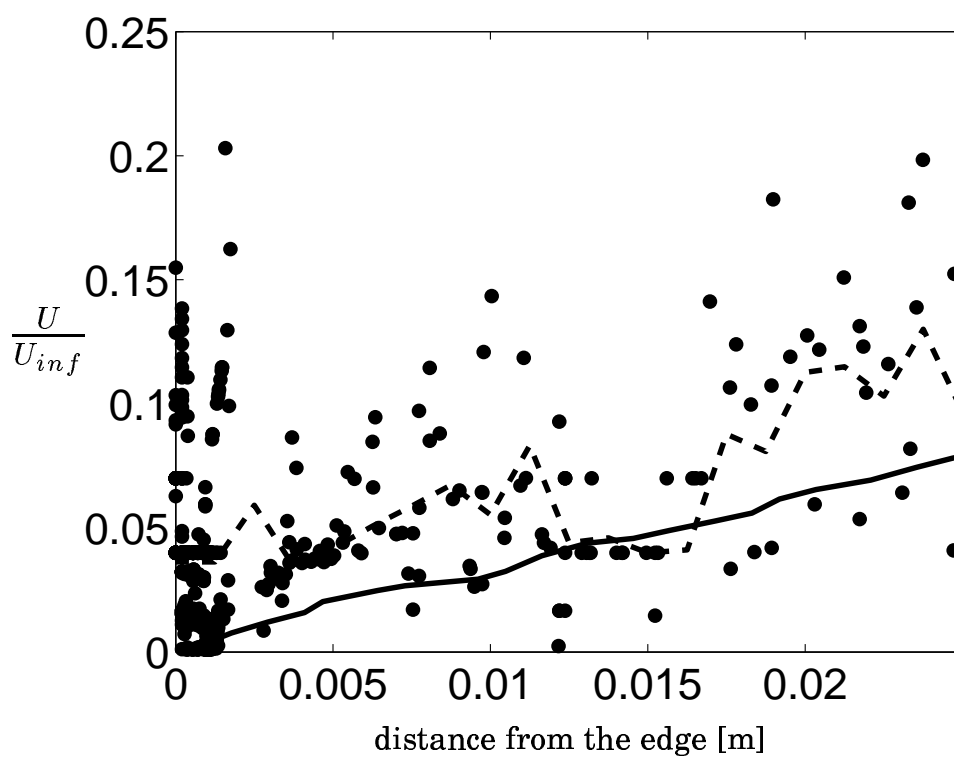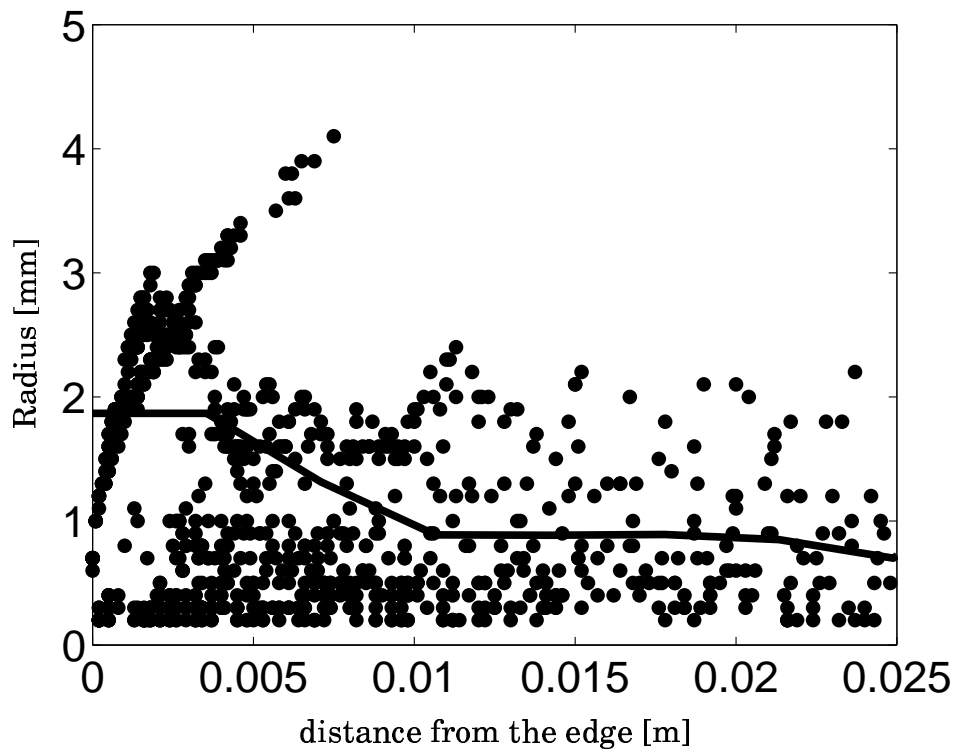
Figure 5.20: Velocity of the droplets for 40 km/h . Dots: predictions; dashed line: computed average; solid line: experimental data.
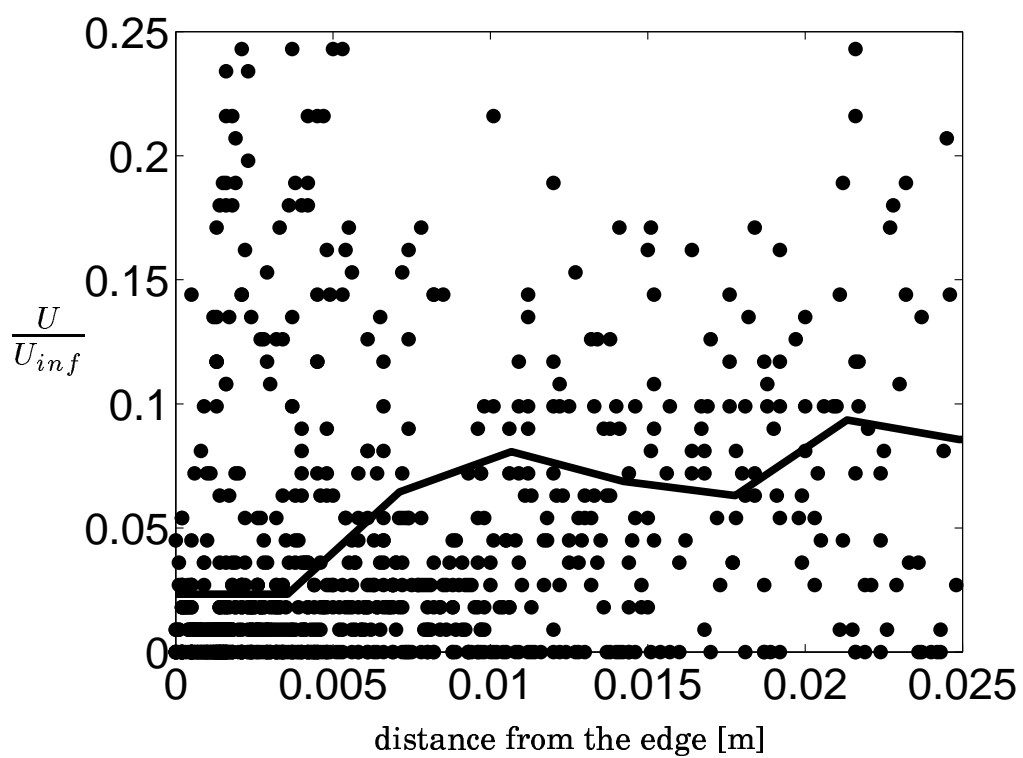
Figure 5.21: Radius of the droplets for 70 km/h . Dots: predictions; dashed line: computed average; solid line: experimental data.
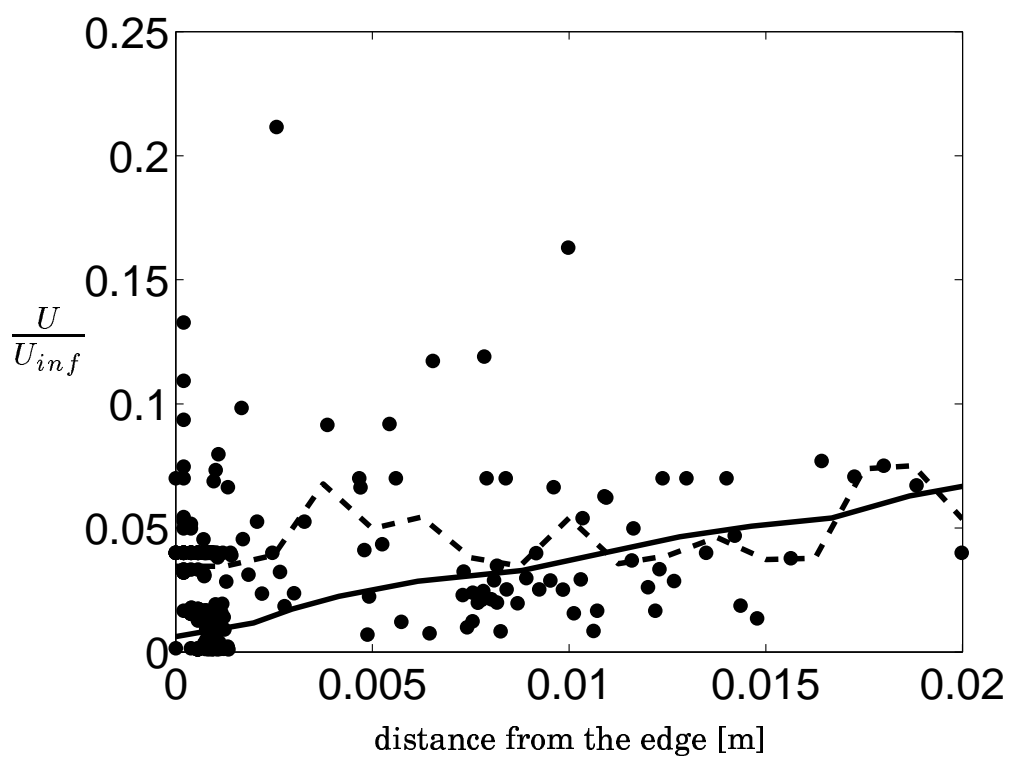
Figure 5.22: Velocity of the droplets for 70 km/h. Dots: predictions; dashed line: computed average; solid line: experimental data.

Figure 5.23: Radius of the droplets for 40 km/h. Solid line: experimental average; dots: experimental data.

Figure 5.24: Velocity of the droplets for 40 km/h. Solid line: experimental average; Dots: experimental data.

Chapter 6

Conclusions

The main idea from the beginning is to use Lagrange particle tracking where the shape of the droplets was unimportant and VOF where it is important. It was found that it has some good features and some bad. VOF is very good theoretically, infact almost perfect. VOF could handle everything we want: drag, surface tension, break-up etc. The results from a gravity driven rivulet are good, and results from the shear driven rivulet are also fairly good. However, it has some major drawbacks.

The complete set of equations takes a very long time to solve with VOF; a CFL number around 0.3 is needed and the solver needs sub-iterations to reach convergence. An estimation is that it takes five times longer using VOF then not using it. The algorithm is very unstable if a high density ratio, surface tension and small dimensions are used. This will lead to very large differences in magnitude for the terms in the equations, as we see in Fig. 4.11. This will many times lead to numerical problems.

The sharpest VOF scheme was many times impossible to get to converge, and the more diffusive schemes usually became too diffusive.

To get a good VOF solution without too many convergence problems,a much smaller time step than a CFL of 0.3 is needed most of the time. The conclusion is that VOF can not be used in industry for this purpose, as it is very time consuming and too unstable. An alternative is thin liquid film models, which are much less theoretically accurate but have some good features. Film models are more stable and faster (usually one-way coupling). The drawback is that film models can not break up on their own; one need to put some constains must be specified

Bibliography

ATAKI, A. & BART, H. 2004 The use of vof-model to study the wetting of solide surface. *Chemical Engineering and Technology* **27** (10), 1109–1114.

BRACKBILL, J., KOTHE, D. B. & ZEMACH, C. 1992 A continuum method for modeling surface tension. *Journal of Computational Physics* **1**, 335–354.

FLUENT 2006 Fluent 6.3 users guide, fluent inc.

HIRT, C. & NICHOLS, B. 1981 Volume of fluid (vof) method for the dynamics of free boundaries. *Journal of Computational Physics* **39**, 201–225.

LAFUENTE, J. M. 2007 Experimental studies of water management on a flat plate and simplified rear view mirror. MSc Thesis 07/15. Division of Fluid Dynamics, Departmwent of Applied Mechanics, Chalmers University of Technology, Göteborg, Sweden.

MUZAFERIJU, S. & PERIC, M. 2000 A two-fluid Navier-Stokes solver to simulate water entry. In *22nd Symposium on Naval Hydrodynamics*, pp. 638–651.

UBBINK, O. 1997 Numerical prediction of two fluid systems with sharp interfaces. PhD thesis, Imperial College of Science, Technology and Medicine, London.

UNIVERDI, S. & TRYGGVESON, G. 2001 A front-tracking method for the computations of multiphase flow. *Journal of Computational Physics* **169**, 708–759.

YOUNGS, D. L. 1982 Time-dependent multi-material flow with large fluid distortion. *Numerical Methods for Fluid Dynamics. Academic Press* pp. 273–285.